

Waveform inversion for parameters of microseismic sources in VTI media

Oscar Jarillo Michel and Ilya Tsvankin

Center for Wave Phenomena, Colorado School of Mines

ABSTRACT

Waveform inversion (WI), which has been used primarily for high-resolution velocity analysis, can also be employed to obtain the source parameters of microseismic events. Here, we implement WI to estimate the location, origin time, and seismic moment tensor of microseismic sources embedded in VTI (transversely isotropic with a vertical symmetry axis) media. The algorithm operates with multicomponent wavefields modeled using an elastic anisotropic finite-difference code. The gradient of the objective function for the three classes of parameters is calculated with the adjoint-state method. Although in the current algorithm the interval VTI parameters are assumed to be known, they can be included in WI at almost no additional cost. Synthetic tests for data recorded by vertical receiver arrays show that it is possible to tightly constrain all source parameters, if a sufficiently accurate initial model is available. In particular, the source location in layered VTI media can be estimated simultaneously with the moment tensor. The resolution of event location, however, somewhat decreases when the origin time is unknown or there is an error in one of the VTI parameters.

1 INTRODUCTION

Waveform inversion is a nonlinear optimization technique based on full-wavefield modeling, which is designed to include the entire seismic trace in building subsurface models. As first suggested by Lailly (1983) and Tarantola (1984), back-propagation in time of the data residuals followed by cross-correlation of the resulting wavefield with the forward-propagated wavefield helps iteratively produce high-resolution velocity models. An overview of the progress in WI methods can be found in Virieux and Operto (2009). Applications of WI in exploration seismology have been mostly limited to velocity tomography. Seismic waveforms, however, contain information that can be used to constrain other important quantities, such as parameters of earthquake sources.

Recently, waveform inversion has been extended to elastic and anisotropic media (Kamath and Tsvankin, 2013), which makes it appropriate for multicomponent reflection and microseismic data. Also, WI has been employed to estimate earthquake source parameters in global seismology (Tromp et al., 2005; Liu and Tromp, 2006; Kim et al., 2011) and geothermal studies (Morency and Mellors, 2012). These techniques incorporate the adjoint-state method (Lions, 1972; Plessix, 2006; Fichtner, 2006, 2009) as a practical way to calculate the gradient of the WI objective function. The main advantage of this method (Talagrand and Courtier, 1987) is that the gradient for all model parameters is computed using only two numerical-modeling simulations. Employing the approach described in Kim et al. (2011), Jarillo Michel and Tsvankin (2014; hereafter referred to as Paper I) implemented gradient

calculation in WI for the source location and moment tensor of a microseismic event in a 2D VTI medium. Their results show that the adjoint wavefield can also be used to identify the presence of missed sources and, in general, improve the initial source position for WI.

Microseismic monitoring of hydraulic fractures has become an important technology in the development of unconventional shale reservoirs (Maxwell, 2010; Kendall et al., 2011). Whereas the main goal of microseismic surveys is to estimate the source locations \mathbf{x}^s , it is also essential to obtain the event origin time t_0 and the source moment tensor \mathbf{M} . Most existing techniques invert for these quantities separately; for instance, the tensor \mathbf{M} is often estimated under the assumption that \mathbf{x}^s is known. In contrast, WI has the potential of resolving all these parameters simultaneously and with high accuracy from multicomponent seismic data.

Here, we present a 2D methodology for estimating the parameters \mathbf{x}^s , t_0 , and \mathbf{M} using waveform inversion. First, calculation of the gradient of the objective function is implemented for heterogeneous VTI media using the approach developed in Paper I. Wavefields from dislocation-type microseismic sources are generated with a 2D elastic finite-difference algorithm. Then we introduce an iterative local gradient-descent algorithm for simultaneous updating of all source parameters. The inversion involves the so-called nondimensionalization approach (Kim et al., 2011) because the model parameters belong to different classes (i.e., have different units). Finally, the methodology is tested on multicomponent data generated for

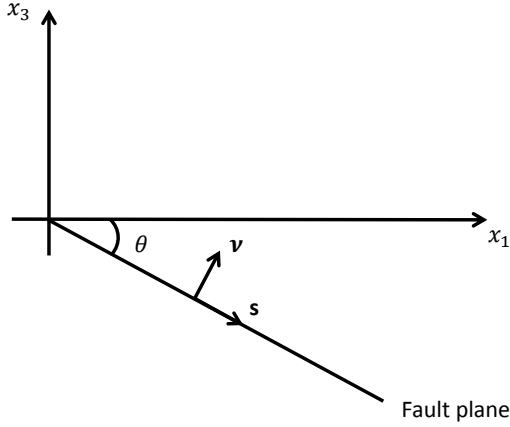


Figure 1. 2D fault geometry used in forward modeling. The vector \mathbf{v} is the unit fault normal, and \mathbf{s} is a unit vector in the slip direction. The dip angle θ ($0^\circ \leq \theta \leq 90^\circ$) is measured down from the horizontal axis. The incidence plane $[x_1, x_3]$ is assumed to coincide with the dip plane of the fault and contain the slip \mathbf{s} .

four different microseismic experiments in homogeneous and horizontally layered VTI media.

2 INVERSE PROBLEM

The wave equation for a seismic source located at point \mathbf{x}^s in heterogeneous anisotropic media can be written as (Aki and Richards, 2002):

$$\rho \frac{\partial^2 u_i}{\partial t^2} - \frac{\partial}{\partial x_j} \left(c_{ijkl} \frac{\partial u_k}{\partial x_l} \right) = -M_{ij} \frac{\partial [\delta(\mathbf{x} - \mathbf{x}^s)]}{\partial x_j} S(t), \quad (1)$$

where $\mathbf{u}(\mathbf{x}, t)$ is the displacement field, t is time, c_{ijkl} is the stiffness tensor ($i, j, k, l = 1, 2, 3$), $\rho(\mathbf{x})$ is the density, M_{ij} is the seismic moment tensor, $S(t)$ is the source time function, and $\delta(\mathbf{x} - \mathbf{x}^s)$ is the spatial δ -function; summation over repeated indices is implied. We use finite-difference (FD) algorithm `sfewe` in `MADAGASCAR` to obtain the exact wavefield from equation 1. P- and SV-waves that propagate in the $[x_1, x_3]$ -plane depend on the components M_{11} , M_{13} , and M_{33} of the moment tensor, which can be represented as a function of the fault dip angle θ (Figure 1; see Paper I):

$$M_{11} = -\frac{\Sigma \bar{u}}{2} (c_{13} - c_{11}) \sin 2\theta, \quad (2)$$

$$M_{13} = \Sigma \bar{u} c_{55} \cos 2\theta, \quad (3)$$

$$M_{33} = -\frac{\Sigma \bar{u}}{2} (c_{33} - c_{13}) \sin 2\theta, \quad (4)$$

where Σ is the fault area, \bar{u} is the magnitude of the slip (displacement discontinuity), and c_{11} , c_{13} , c_{33} , and c_{55} are the stiffness coefficients in the two-index Voigt notation.

Here, our goal is to invert for the source coordinates x_1^s and x_3^s , the origin time t_0 , and the three relevant moment-tensor elements assuming that the velocity model is known. Hence, the vector of unknown model parameters is defined as:

$$\mathbf{m} = \{x_1^s, x_3^s, t_0, M_{11}, M_{13}, M_{33}\}. \quad (5)$$

In synthetic tests, the observed displacement \mathbf{d}_{obs} and predicted displacement $\mathbf{d}_{\text{pre}}(\mathbf{m})$ are produced by two forward simulations, with \mathbf{d}_{pre} computed after perturbing the source parameters used to generate \mathbf{d}_{obs} . The elastic displacement field $\mathbf{u}(\mathbf{x}^s, \mathbf{x}^n, t)$ in both simulations is excited by a single source at \mathbf{x}^s and recorded by N receivers located at \mathbf{x}^n ($n = 1, 2, \dots, N$). The data residuals are measured by the least-squares objective function \mathcal{F} , which is minimized by the inversion algorithm:

$$\mathcal{F}(\mathbf{m}) = \frac{1}{2} \|\mathbf{d}_{\text{pre}}(\mathbf{m}) - \mathbf{d}_{\text{obs}}\|^2. \quad (6)$$

3 APPLICATION OF THE ADJOINT-STATE METHOD

The adjoint-state method is designed to efficiently calculate the derivatives of the objective function with respect to the model parameters, $\partial \mathcal{F}(\mathbf{m}) / \partial \mathbf{m}$. Computation of the gradient of the objective function for our problem is discussed in Paper I. In addition to equation 1, the method requires solving the adjoint wave equation:

$$\rho \frac{\partial^2 u_i^\dagger}{\partial t^2} - \frac{\partial}{\partial x_j} \left(c_{ijkl} \frac{\partial u_k^\dagger}{\partial x_l} \right) = \sum_{n=1}^N (\mathbf{d}_{\text{obs}} - \mathbf{d}_{\text{pre}})(T-t) \delta(\mathbf{x} - \mathbf{x}^n), \quad (7)$$

where \mathbf{u}^\dagger is called the ‘‘adjoint wavefield.’’ The ‘‘adjoint source’’ on the right-hand side of equation 7 consists of the time-reversed data residuals and is obtained by differentiating $\mathcal{F}(\mathbf{m})$ with respect to the forward wavefield \mathbf{u} . The adjoint simulation to generate \mathbf{u}^\dagger can be carried out with the forward-modeling code that solves equation 1 by using the receivers as simultaneous adjoint sources.

The derivatives of the objective function with respect to the source coordinates, origin time, and moment-tensor elements can be found as (Kim et al., 2011; Paper I):

$$g_{x_i^s} = \frac{\partial \mathcal{F}}{\partial x_i^s} = \int_0^T \frac{\partial [\mathbf{M} : \boldsymbol{\epsilon}^\dagger(\mathbf{x}^{\text{ts}}, t)]}{\partial x_i} \Big|_{\mathbf{x}^{\text{ts}}} S(T-t) dt, \quad (8)$$

$$g_{t_0} = \frac{\partial \mathcal{F}}{\partial t_0} = \int_0^T \mathbf{M} : \boldsymbol{\epsilon}^\dagger(\mathbf{x}^{\text{ts}}, t) \frac{\partial S(T-t)}{\partial t} dt, \quad (9)$$

$$g_{M_{ij}} = \frac{\partial \mathcal{F}}{\partial M_{ij}} = \int_0^T \boldsymbol{\epsilon}_{ij}^\dagger(\mathbf{x}^{\text{ts}}, t) S(T-t) dt, \quad (10)$$

where \mathbf{x}^{ts} is the trial source location, T is the recording time, $\boldsymbol{\varepsilon}^\dagger = \frac{1}{2}[\nabla\mathbf{u}^\dagger + (\nabla\mathbf{u}^\dagger)^T]$ is the adjoint strain tensor, and $\mathbf{M} : \boldsymbol{\varepsilon}^\dagger$ is the double inner product of the tensors \mathbf{M} and $\boldsymbol{\varepsilon}^\dagger$. Equations 8 – 10 applied to the 2D problem at hand yield the gradient vector \mathbf{g} for the six source parameters:

$$\mathbf{g} = \left\{ \frac{\partial \mathcal{F}}{\partial x_1^s}, \frac{\partial \mathcal{F}}{\partial x_3^s}, \frac{\partial \mathcal{F}}{\partial t_0}, \frac{\partial \mathcal{F}}{\partial M_{11}}, \frac{\partial \mathcal{F}}{\partial M_{13}}, \frac{\partial \mathcal{F}}{\partial M_{33}} \right\}. \quad (11)$$

For inversion purposes, the derivatives in equations 8 – 10 are needed only at the trial source position. Note that the derivatives for \mathbf{x}^s and t_0 (equations 8 and 9) include the double-inner product $\mathbf{M} : \boldsymbol{\varepsilon}^\dagger(\mathbf{x}^{\text{ts}}, t)$, which involves summation over all elements of \mathbf{M} . Due to this dependence, stable inversion for \mathbf{x}^s and t_0 requires an accurate initial model for the moment tensor.

4 IMPLEMENTATION

The model parameters have different units, and local minimization of $\mathcal{F}(\mathbf{m})$ could be performed for each parameter class separately. However, here we carry out simultaneous inversion for \mathbf{x}^s , t_0 , and \mathbf{M} employing the nondimensionalization approach suggested by Kim et al. (2011), which also helps avoid the additional computational cost of multidirectional minimization. This approach eliminates the difference between the units of different parameters classes, which makes possible simultaneous parameter updating. At the first iteration, we define the following scaling coefficients σ for each parameter class:

$$\sigma_{\mathbf{x}^s} = \beta_{\mathbf{x}^s} \frac{1}{\sqrt{g_{x_1^s}^2 + g_{x_3^s}^2}}, \quad (12)$$

$$\sigma_{t_0} = \beta_{t_0} \frac{1}{|g_{t_0}|}, \quad (13)$$

$$\sigma_{\mathbf{M}} = \beta_{\mathbf{M}} \frac{1}{\sqrt{g_{M_{11}}^2 + g_{M_{13}}^2 + g_{M_{33}}^2}}, \quad (14)$$

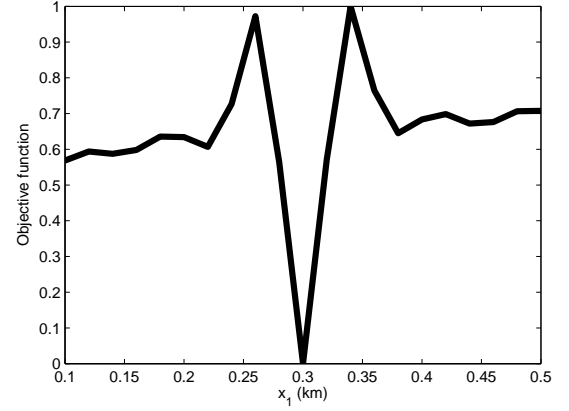
where the quantities $\beta_{\mathbf{x}^s}$, $\beta_{\mathbf{M}}$, and β_{t_0} are scaling factors that ensure that each parameter class gives a comparable contribution to the gradient. These factors may be different for each experiment and can be determined, for instance, by evaluating the change in the gradient produced by β_c (c indicates the parameter class) between the first and second iteration. The “nondimensionalized” model parameters are:

$$\hat{\mathbf{m}}_c = \frac{\mathbf{m}_c}{\sigma_c}. \quad (15)$$

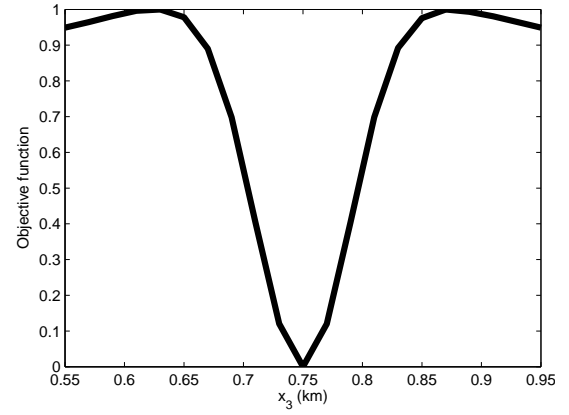
The gradient becomes dimensionless after the following scaling:

$$\hat{\mathbf{g}}_c = \mathbf{g}_c \sigma_c. \quad (16)$$

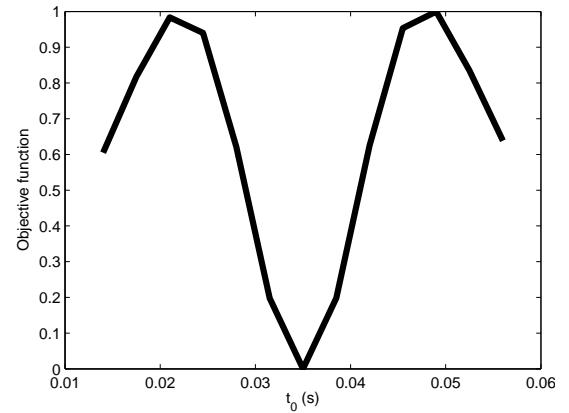
As discussed in more detail below, the inverse problem



(a)



(b)



(c)

Figure 2. Dependence of the objective function $\mathcal{F}(\mathbf{m})$ on the trial source parameters (a) x_1^s , (b) x_3^s , and (c) t_0 for a homogeneous VTI model. The global minimum coincides with the actual parameter value. The components of the tensor \mathbf{M} are fixed at the actual values. Here and below, we describe the medium using the Thomsen parameters — the P- and S-wave vertical velocities (V_{P0} and V_{S0}) and the anisotropy coefficients ε and δ (Thomsen, 1986; Tsvankin, 2012). In this test, $\rho = 2 \text{ g/cm}^3$, $V_{P0} = 4047 \text{ m/s}$, $V_{S0} = 2638 \text{ m/s}$, $\varepsilon = 0.4$, and $\delta = 0$.

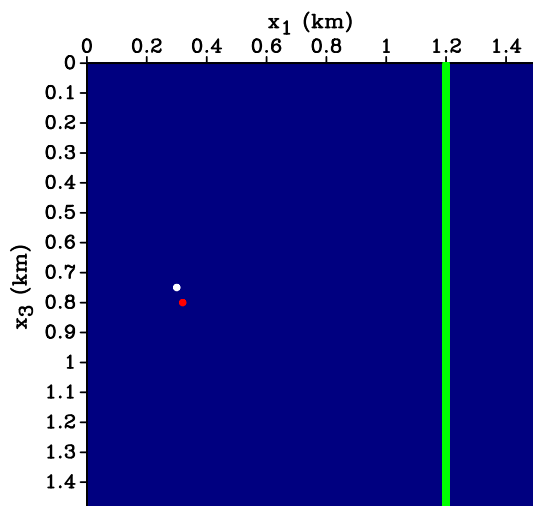


Figure 3. Actual source (white dot), trial source (red dot) and a vertical line of receivers (spacing is 6 m) embedded in a homogeneous VTI medium. The medium parameters are $\rho = 2 \text{ g/cm}^3$, $V_{p0} = 4047 \text{ m/s}$, $V_{S0} = 2638 \text{ m/s}$, $\epsilon = 0.4$, and $\delta = 0$. The actual source is located at $x_1 = 0.3 \text{ km}$ and $x_3 = 0.75 \text{ km}$ with $\theta = 0^\circ$ (see equations 2 – 4). For the trial source, $x_1 = 0.32 \text{ km}$, $x_3 = 0.8 \text{ km}$, and $\theta = 15^\circ$. Both events occur at the same time ($t_0 = 0.049 \text{ s}$).

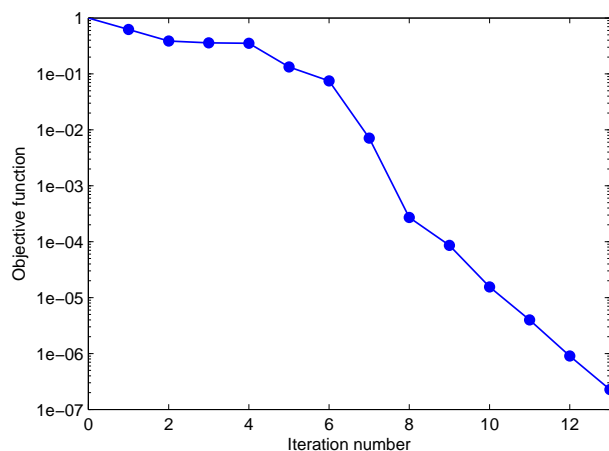
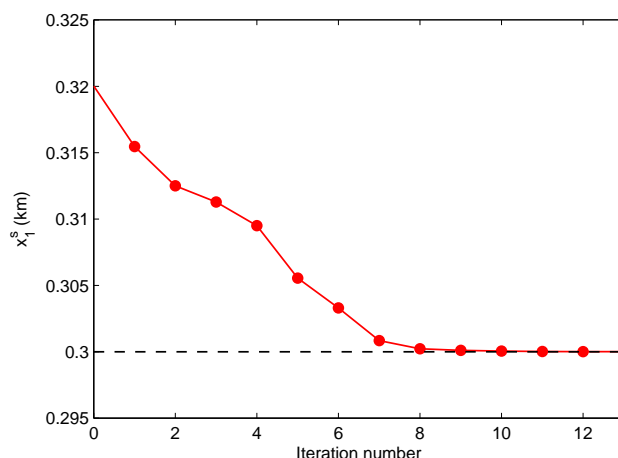
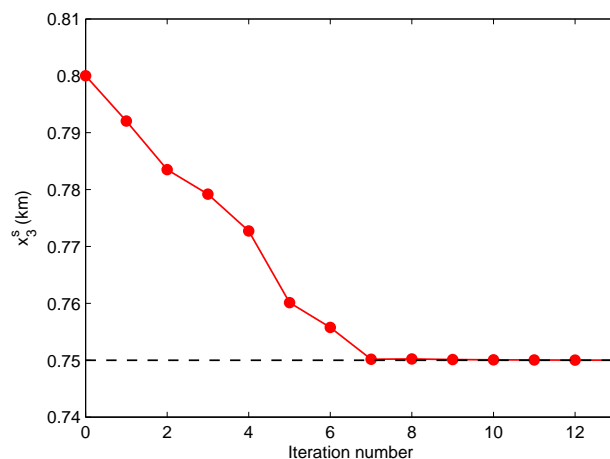


Figure 4. Change of the normalized objective function $\mathcal{F}(\mathbf{m})$ with iterations for the model in Figure 3.

is nonlinear, and we solve it using an iterative local gradient-descent scheme. Suppose the model \mathbf{m}^k is obtained after $k - 1$ iterations of the inversion algorithm. First, the forward simulation is performed to generate the predicted data $\mathbf{d}_{\text{pre}}^k(\mathbf{m}^k)$, which allows us to compute the objective function \mathcal{F}^k . Then, we carry out the adjoint simulation to calculate the gradient \mathbf{g}^k using equations 8 – 10. The next step is nondimensionalization of the model parameters (equation 15) and scaling of the gradient (equation 16). Note that the scaling coefficients



(a)



(b)

Figure 5. Change of the source coordinates (a) x_1^s and (b) x_3^s with iterations for the model in Figure 3. The actual values are marked by dashed lines.

are computed at the first iteration and kept constant during the inversion. Because the nondimensionalized model parameters have the same units (those of \mathcal{F}) and the scaled gradient is dimensionless, the three classes of parameters can be updated simultaneously using a constant step length α :

$$\hat{\mathbf{m}}^{k+1} = \hat{\mathbf{m}}^k + \alpha \hat{\mathbf{g}}^k. \quad (17)$$

Assuming that $\hat{\mathbf{m}}^k$ is located within the basin that contains the global minimum of \mathcal{F} , the step length should be sufficiently small to ensure that $\hat{\mathbf{m}}^{k+1}$ stays within this basin. Using a constant step eliminates the computational cost required to perform a line search for α . After the update, the parameters have to be “dimensionalized” again so that they can be used as inputs for the forward modeling in the next iteration:

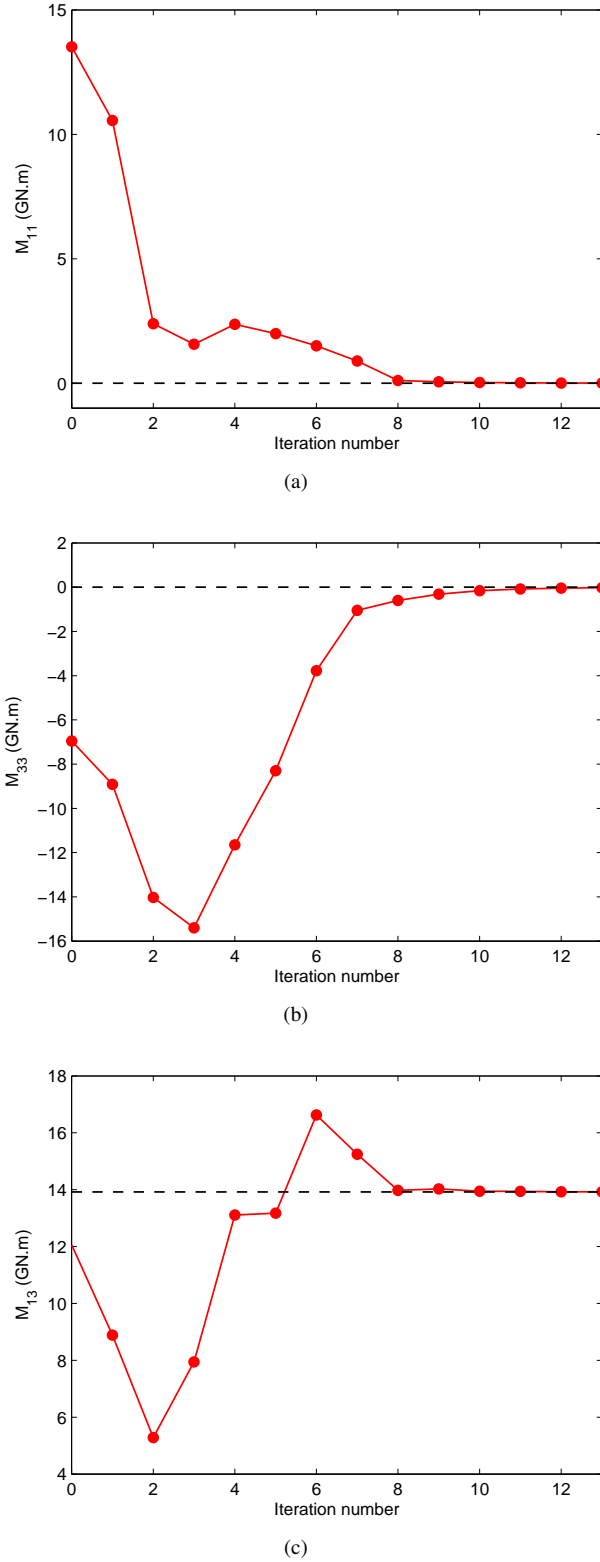


Figure 6. Change of the moment-tensor elements (a) M_{11} , (b) M_{33} , and (c) M_{13} with iterations for the model in Figure 3. The actual values are marked by dashed lines.

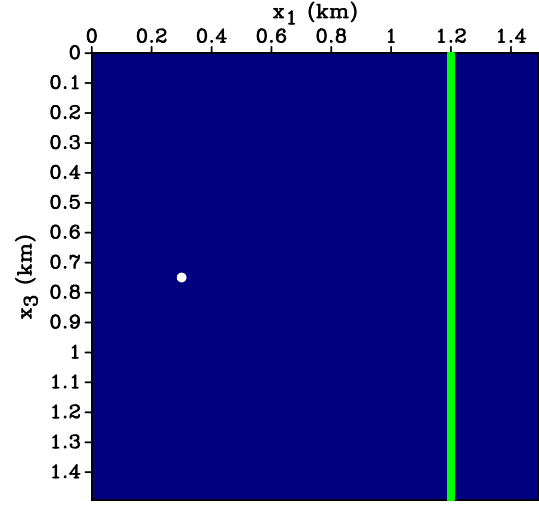


Figure 7. Source (white dot) and a vertical line of receivers (spacing is 6 m) embedded in a homogeneous VTI medium. The medium parameters are the same as in Figure 3. The location of the actual and trial sources is the same: $x_1 = 0.3$ km and $x_3 = 0.75$ km. For the actual source, $t_0 = 0.049$ s and $\theta = 0^\circ$, for the trial source, $t_0 = 0.042$ s and $\theta = 15^\circ$.

$$\mathbf{m}_c^{k+1} = \hat{\mathbf{m}}_c^{k+1} \sigma_c. \quad (18)$$

5 PROPERTIES OF THE INVERSE PROBLEM

Estimating the moment tensor \mathbf{M} of an earthquake from seismic amplitudes is a linear inverse problem. However, simultaneous inversion for \mathbf{M} , \mathbf{x}^s , and t_0 is nonlinear because the recorded data depend on \mathbf{x}^s and t_0 in a nonlinear fashion. The joint inversion for \mathbf{M} , \mathbf{x}^s , and t_0 involves complications typical for velocity estimation using WI. For example, cycle-skipping can occur if the trial model is too far from the actual one or if the step length α used in model updating is too large. In particular, the trial source should be within about one-half of the predominant wavelength from the actual source location.

Figure 2 shows the variation of the normalized objective function with the coordinates \mathbf{x}^s and time t_0 . To ensure convergence to the actual values, the trial model should lie within the basin that contains the global minimum. If the inversion involves simultaneous estimation of x_1^s , x_3^s , and t_0 , the basin containing the global minimum in the plots of Figure 2 becomes more narrow, which increases the risk of cycle skipping.

6 NUMERICAL RESULTS

Here, we present synthetic tests of the WI algorithm for a homogeneous VTI medium and a stack of horizontal VTI layers. In all experiments, the observed data are generated by a single microseismic event recorded by a vertical array of closely spaced receivers.

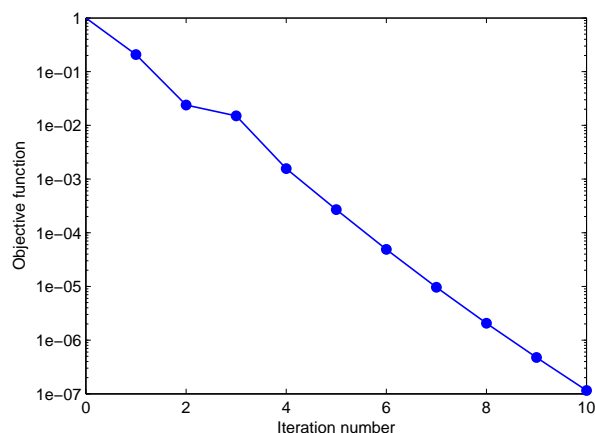


Figure 8. Change of the normalized objective function $\mathcal{F}(\mathbf{m})$ with iterations for the model in Figure 7.

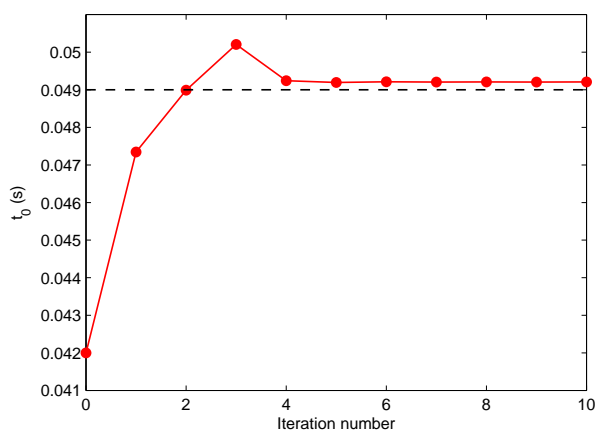
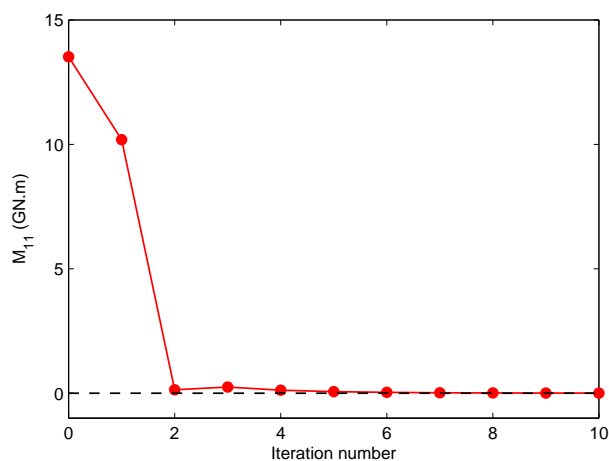


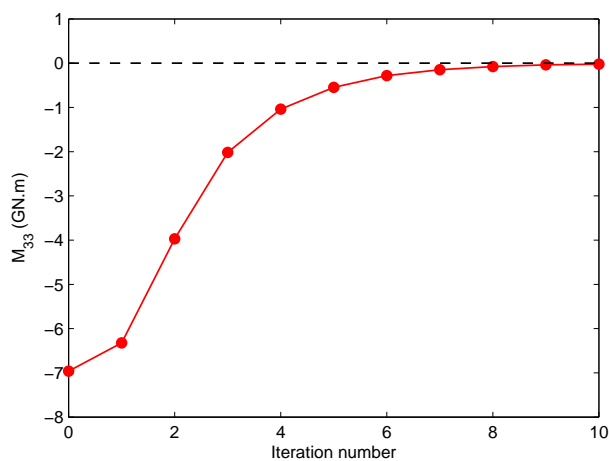
Figure 9. Change of the origin time t_0 with iterations for the model in Figure 7.

In the first experiment, we invert for the parameters x_1^s , x_3^s , M_{11} , M_{13} , and M_{33} with the origin time t_0 fixed at the actual value (Figure 3). Because the medium is homogeneous, the wavefield is composed just of the direct P- and SV-waves. The objective function becomes practically negligible after about 10 iterations (Figure 4). The moment tensor and source coordinates are estimated with high accuracy (Figures 5 and 6), with the errors in x_1^s and x_3^s on the order of centimeters. Note that the algorithm was able to resolve the moment tensor \mathbf{M} , although the data were acquired in a single vertical borehole. The pronounced variations in \mathbf{M} during the initial iterations are due to the incorrect position of the source, which produces large changes in the amplitudes of the P- and SV-waves.

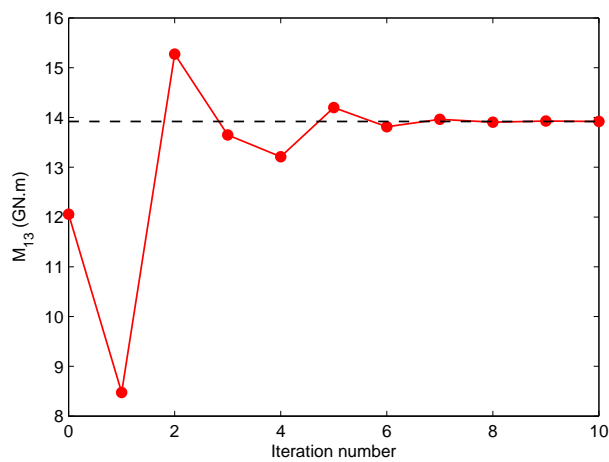
In the second test, the origin time t_0 is perturbed, while the location \mathbf{x}^s is fixed at the correct value (Figure 7). The tensor \mathbf{M} is perturbed in the same way as in the previous example.



(a)



(b)



(c)

Figure 10. Change of the moment-tensor elements (a) M_{11} , (b) M_{33} , and (c) M_{13} with iterations for the model in Figure 7.

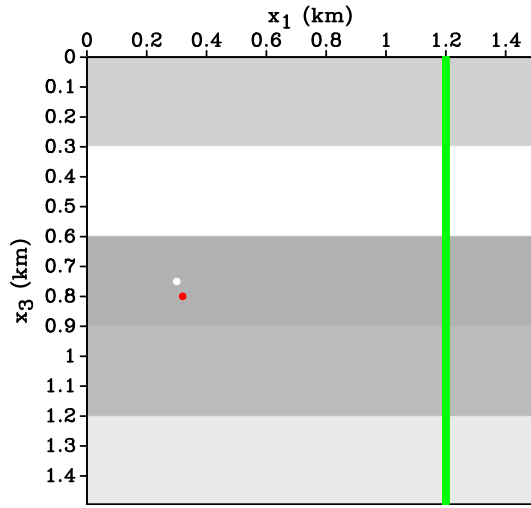


Figure 11. Actual (white dot) and trial (red dot) sources and a vertical receiver array in a five-layer VTI model. The receiver geometry is the same as in Figure 3. The parameters $\rho = 2 \text{ kg/m}^3$, $\epsilon = 0.4$, and $\delta = 0$ are the same in all five layers. The vertical velocities in the top layer are $V_{P0} = 4419 \text{ m/s}$ and $V_{S0} = 2645 \text{ m/s}$; for the second layer, $V_{P0} = 4956 \text{ m/s}$ and $V_{S0} = 2424 \text{ m/s}$; for the third layer, $V_{P0} = 4048 \text{ m/s}$ and $V_{S0} = 2638 \text{ m/s}$; for the fourth layer, $V_{P0} = 4170 \text{ m/s}$ and $V_{S0} = 2320 \text{ m/s}$; for the fifth layer, $V_{P0} = 4694 \text{ m/s}$ and $V_{S0} = 2682 \text{ m/s}$. The actual source is located at $x_1 = 0.3 \text{ km}$ and $x_3 = 0.75 \text{ km}$ with $\theta = 0^\circ$. The trial source is located at $x_1 = 0.32 \text{ km}$ and $x_3 = 0.8 \text{ km}$ with $\theta = 15^\circ$. Both events occur at the same time ($t_0 = 0.035 \text{ s}$).

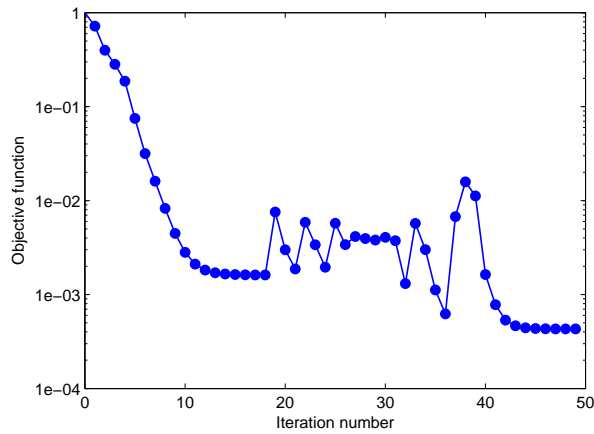
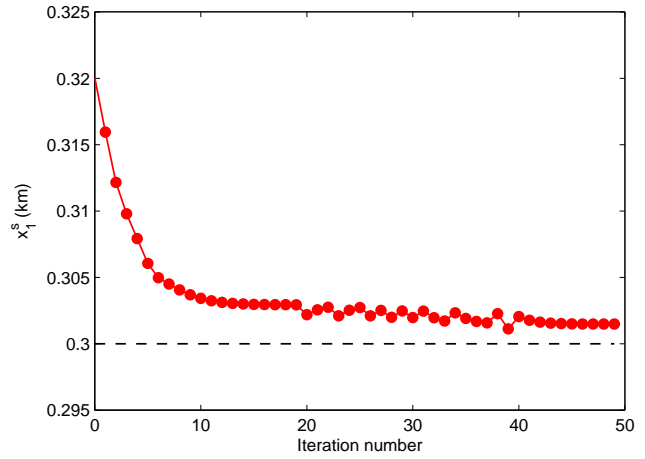


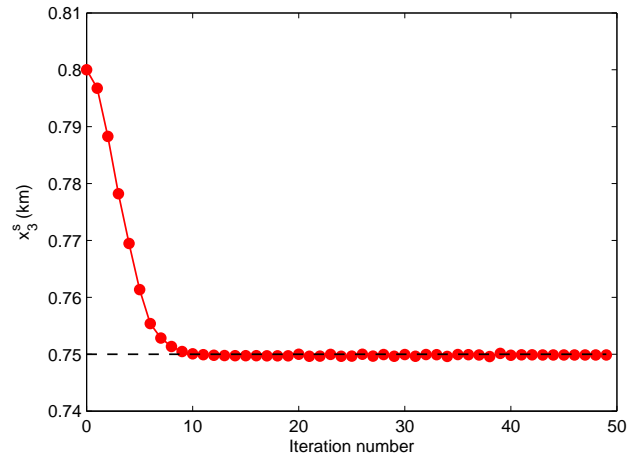
Figure 12. Change of the normalized objective function $\mathcal{F}(\mathbf{m})$ with iterations for the model in Figure 11. All source parameters are unknown.

The rate of the decrease of the objective function (Figure 8) is similar to that in the previous test. The direct P and SV arrivals recorded in a single borehole provide sufficient information to constrain the parameters t_0 and \mathbf{M} (Figures 9 and 10).

Next, we use the five-layer model in Figure 11 and assume that all source parameters (\mathbf{x}^s , t_0 , and \mathbf{M}) are unknown.



(a)



(b)

Figure 13. Change of the source coordinates (a) x_1^s and (b) x_3^s with iterations for the model in Figure 11.

The multiple layers in this model produce numerous scattered waves, which help constrain the source location. Although the origin time t_0 for the actual and trial sources coincides, it varies with iterations as WI tries to match the observed and predicted data.

In theory, moving the source vertically shifts the apex of the P- and S-wave moveouts up or down, with the depth of the apex determining the vertical coordinate x_3^s . Also, variations in the horizontal distance between the source and the receiver array change the difference between the S- and P-wave traveltimes. In contrast, changing the origin time simply shifts the P- and S-wave moveouts along the time axis without moving them in depth or altering their difference. Therefore, the parameters \mathbf{x}^s and t_0 influence the traveltimes in a different way, which should preclude a trade-off between them.

Still, because both \mathbf{x}^s and t_0 are unknown, the objective function oscillates and cannot be reduced as much as in the

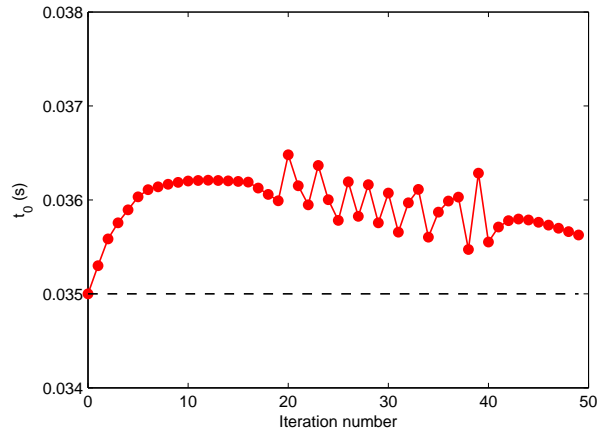


Figure 14. Change of the origin time t_0 with iterations for the model in Figure 11.

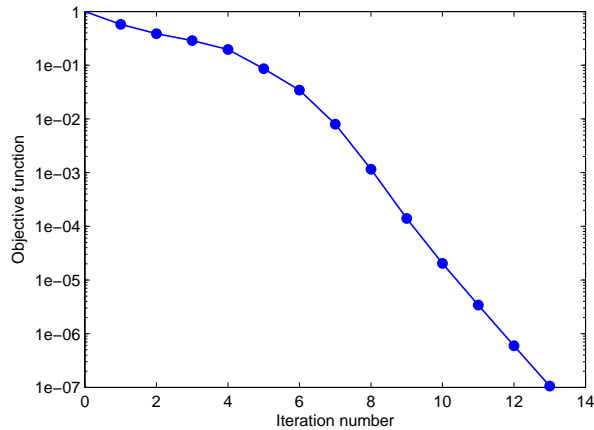
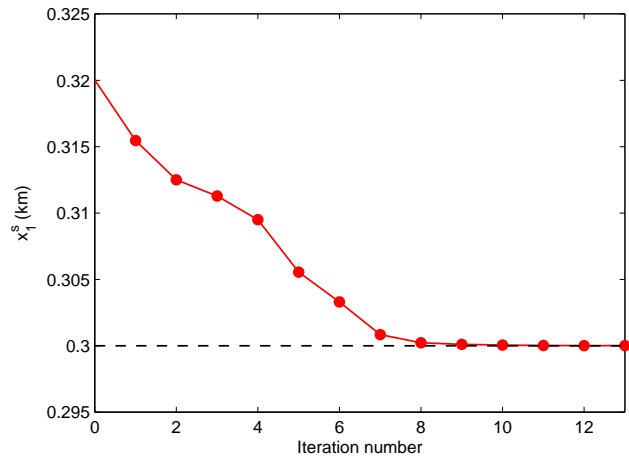


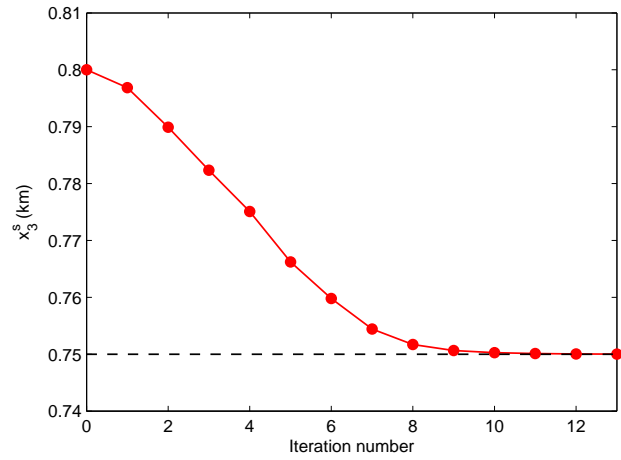
Figure 15. Change of the normalized objective function $\mathcal{F}(\mathbf{m})$ with iterations for the model in Figure 11. The origin time t_0 is fixed at the correct value.

previous examples (Figure 12). After a number of iterations, the estimated \mathbf{x}^s and t_0 are close to the actual parameters. As a result, the P- and SV-traveltime shifts produced by further perturbations in the source location and origin time become too small to guide the inversion toward the actual model. Hence, the obtained horizontal source coordinate x_1^s and time t_0 are slightly distorted (Figures 13 and 14), and the objective function for the inverted model is somewhat larger than that for the first two tests.

In the fourth experiment we use the model in Figure 11, but invert only for \mathbf{M} and \mathbf{x}^s , with the origin time t_0 fixed at the correct value. The objective function rapidly decays with iterations (Figure 15), and the estimated source location is almost exact (Figure 16). Also, we obtain an accurate estimate of all three elements of the tensor \mathbf{M} (Figure 17).



(a)



(b)

Figure 16. Change of the source coordinates (a) x_1^s and (b) x_3^s with iterations for the model in Figure 11. The origin time t_0 is fixed at the correct value.

The previous tests assumed the correct velocity model for WI. In the last example we evaluate the influence of velocity errors on the inversion results by distorting the anisotropy coefficient ϵ for the homogeneous VTI model in Figure 3. The algorithm estimates the parameters \mathbf{x}^s and \mathbf{M} , whereas the origin time t_0 is fixed at the actual value. In particular, an error in ϵ changes the P-wave horizontal velocity V_{hor} , which should influence estimation of the horizontal source coordinate x_1^s . After a fast initial decrease, the objective function flattens out (Figure 18) at a larger value than that in Figure 4. Still, errors in the source coordinates are relatively small (about 5 m for x_1^s), and the elements M_{11} and M_{33} of the moment tensor are also recovered with high accuracy. However, there is a more significant error (over 20%) in the element M_{13} , which is most sensitive to the quality of waveform matching.

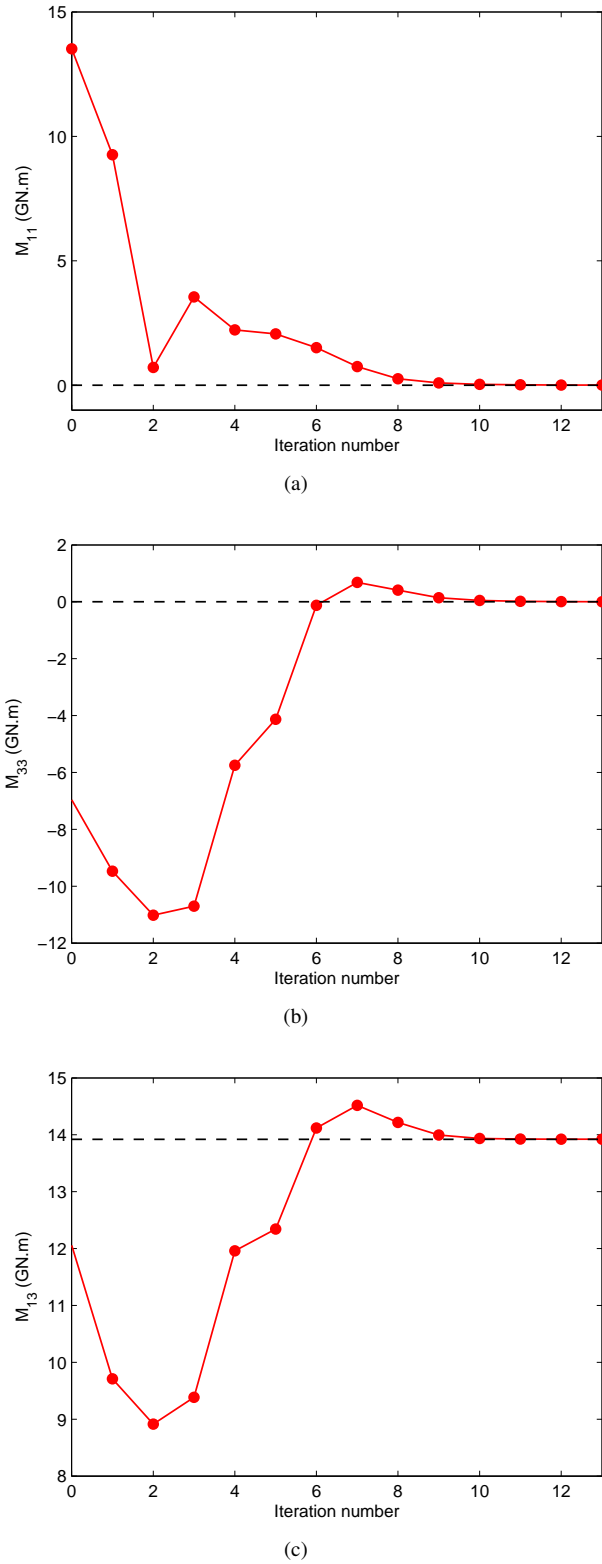


Figure 17. Change of the moment-tensor elements (a) M_{11} , (b) M_{33} , and (c) M_{13} with iterations for the model in Figure 11. The origin time t_0 is fixed at the correct value.

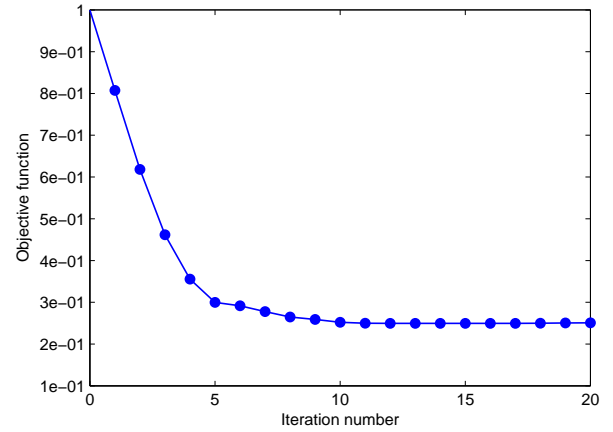


Figure 18. Change of the normalized objective function $\mathcal{F}(\mathbf{m})$ with iterations for the model in Figure 3. The inversion is performed with an incorrect value of ε ($\varepsilon = 0.3$ instead of the actual 0.4). The rest of the VTI parameters are unchanged.

7 CONCLUSIONS

We presented a waveform-inversion methodology for estimating the source parameters (location \mathbf{x}^s , origin time t_0 , and moment tensor \mathbf{M}) of microseismic events from multicomponent data. The WI algorithm operates with the elastic anisotropic wave equation and is designed for dislocation-type sources embedded in 2D heterogeneous VTI media. In addition to employing the entire trace, our method simultaneously inverts for parameters that are typically obtained separately by kinematic and amplitude techniques.

The gradient of the objective function was computed with the adjoint-state method, which requires only two modeling simulations. We employed the nondimensionalization approach to handle model updating for different parameter classes. Although the VTI parameters were assumed known, they can be included in the adjoint calculation. Whereas reconstruction of the velocity model does not substantially increase the computational cost, it can create trade-offs in the inversion.

Synthetic tests were performed for data recorded by a dense vertical array of two-component receivers in homogeneous and horizontally layered VTI media. Increasing the number of layers is actually beneficial for our algorithm because multiple reflections and conversions improve the sensitivity of WI to the source parameters. If the initial model is located within the basin of convergence, WI accurately estimates the parameters \mathbf{x}^s , t_0 , and \mathbf{M} , especially if the origin time is fixed at the correct value. Although in theory there is no trade-off between \mathbf{x}^s and t_0 , the P- and SV-wave traveltime differences responsible for resolving them are small near the global minimum. Our testing shows that simultaneous inversion for the source coordinates and origin time may lead to small distortions in x_1^s and t_0 .

To evaluate the influence of errors in the velocity model, we estimated the parameters of a source in a homogeneous

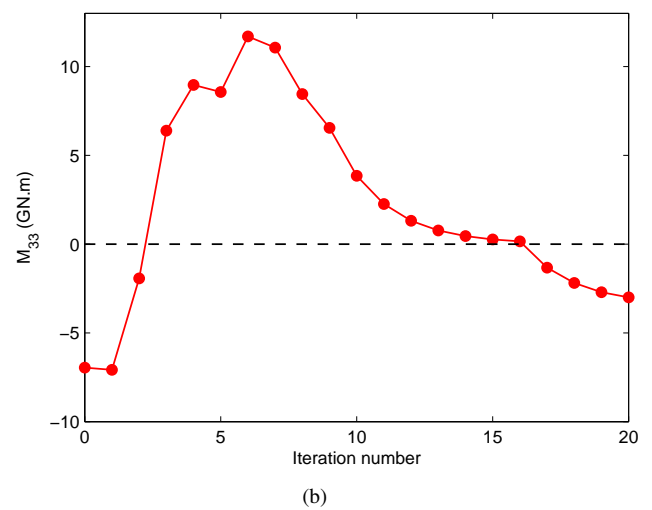
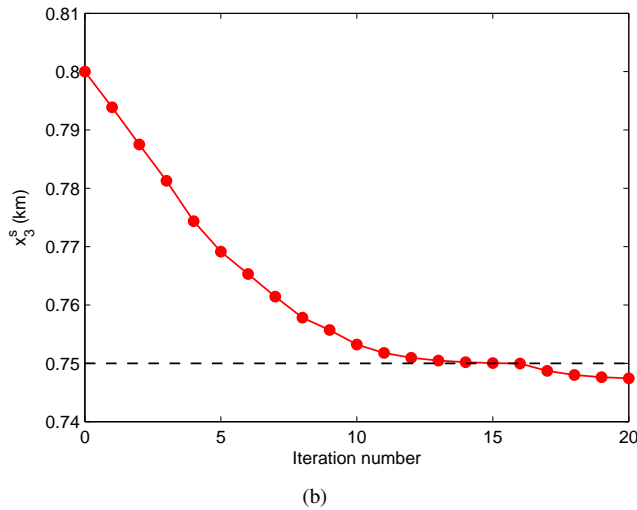
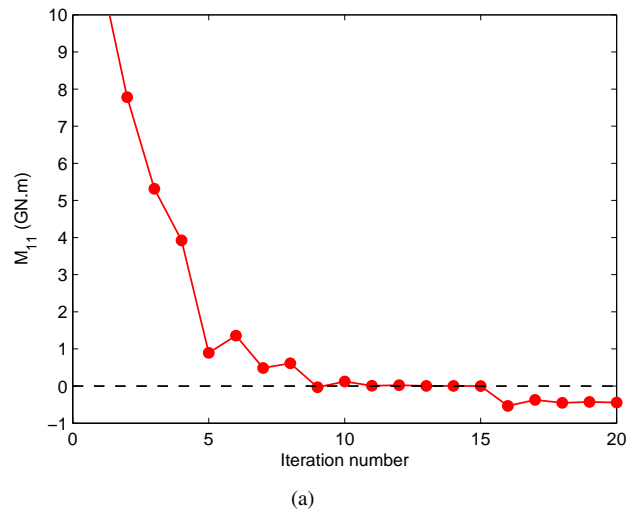
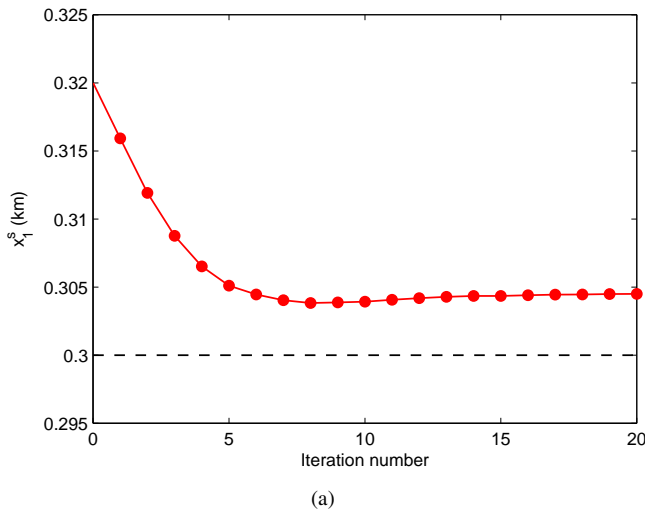


Figure 19. Change of the source coordinates (a) x_1^s and (b) x_3^s with iterations for the model in Figure 3. The inversion uses $\epsilon = 0.3$ instead of the actual $\epsilon = 0.4$.

VTI medium using an inaccurate anisotropy parameter ϵ (0.3 instead of 0.4). Predictably, a distortion in ϵ propagates into the horizontal source coordinate, but the error in x_1^s is not significant; the parameters x_3^s and \mathbf{M} were determined with high accuracy.

To take full advantage of WI and the adjoint-state method in microseismic monitoring, they should be extended to anisotropic velocity model building. As is done in kinematic inversion, anisotropic parameter estimation can be performed simultaneously with event location. These ideas will be discussed in a future publication.

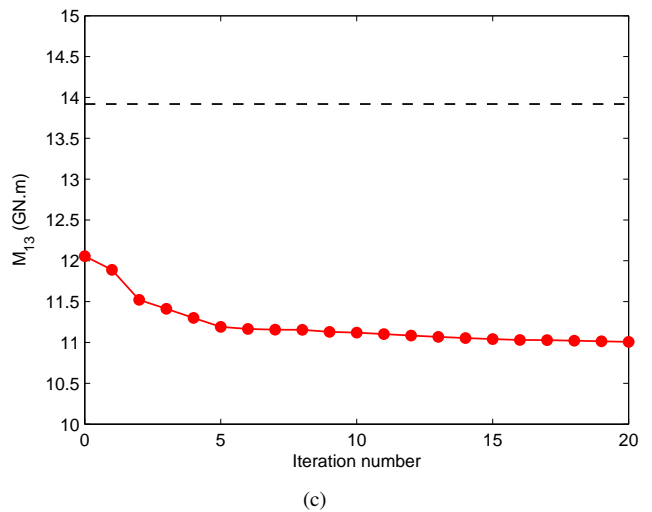


Figure 20. Change of the moment-tensor elements (a) M_{11} , (b) M_{33} , and (c) M_{13} with iterations for the model in Figure 3. The inversion uses $\epsilon = 0.3$ instead of the actual $\epsilon = 0.4$.

8 ACKNOWLEDGMENTS

We are grateful to Vladimir Grechka (Marathon Oil), who generously provided valuable insights and feedback regarding various aspects of this work, and to Jeroen Tromp (Princeton University) for his advice on gradient calculation. We thank Esteban Díaz Pantin and Nishant Kamath (both from CWP) for their technical assistance with the inversion algorithm. The numerical examples in this paper are produced with the **MADAGASCAR** open-source software package freely available at www.ahay.org. This work was supported by the Consortium Project on Seismic Inverse Methods for Complex Structures at the Center for Wave Phenomena (CWP).

REFERENCES

- Aki, K., and P. G. Richards, 2002, *Quantitative seismology*, second ed.: University Science Books.
- Fichtner, A., 2006, The adjoint method in seismology: I. Theory: *Physics of the Earth and Planetary Interiors*, **157**, 86–104.
- , 2009, Full seismic waveform inversion for structural and source parameters: PhD thesis, Ludwig-Maximilians-Universität München.
- Jarillo Michel, O., and I. Tsvankin, 2014, Gradient calculation for waveform inversion of microseismic data in VTI media: CWP Project Review Report.
- Kamath, N., and I. Tsvankin, 2013, Full-waveform inversion of multicomponent data for horizontally layered VTI media: *Geophysics*, **78**, WC113–WC121.
- Kendall, M., S. Maxwell, G. Foulger, L. Eisner, and Z. Lawrence, 2011, Microseismicity: Beyond dots in a box Introduction: *Geophysics*, **76**, WC1–WC3.
- Kim, Y., Q. Liu, and J. Tromp, 2011, Adjoint centroid-moment tensor inversions: *Geophysical Journal International*, **186**, 264–278.
- Lailly, P., 1983, The seismic inverse problem as a sequence of before stack migrations: Bednar, J. B., Redner, R., Robinson, E., and Weglein, A., Eds., *Conference on Inverse Scattering: Theory and Application*, Soc. Industr. Appl. Math., 206–220.
- Lions, J., 1972, *Nonhomogeneous boundary value problems and applications*: Springer Verlag, Berlin.
- Liu, Q., and J. Tromp, 2006, Finite-frequency kernels based on adjoint methods: *Bulletin of the Seismological Society of America*, **96**, 2383–2397.
- Maxwell, S., 2010, Microseismic: Growth born from success: *The Leading Edge*, **29**, 338–343.
- Morency, C., and R. J. Mellors, 2012, Full moment tensor and source location inversion based on full waveform adjoint inversion: application at the Geysers geothermal field: SEG Technical Program Expanded Abstracts, 532, 1–5.
- Plessix, R.-E., 2006, A review of the adjoint-state method for computing the gradient of a functional with geophysical applications: *Geophysical Journal International*, **167**, 495–503.
- Talagrand, O., and P. Courtier, 1987, Variational assimilation of meteorological observations with the adjoint vorticity equation. I: Theory: *Quarterly Journal of the Royal Meteorological Society*, **113**, 1311–1328.
- Tarantola, A., 1984, Inversion of seismic reflection data in the acoustic approximation: *Geophysics*, **49**, 1259–1266.
- Thomsen, L., 1986, Weak elastic anisotropy: *Geophysics*, **51**, 1954–1966.
- Tromp, J., C. Tape, and Q. Liu, 2005, Seismic tomography, adjoint methods, time reversal and banana-doughnut kernels: *Geophysical Journal International*, **160**, 195–216.
- Tsvankin, I., 2012, *Seismic signatures and analysis of reflection data in anisotropic media*, third edition: Society of Exploration Geophysicists.
- Virieux, J., and S. Operto, 2009, An overview of full-waveform inversion in exploration geophysics: *Geophysics*, **74**, WCC1–WCC26.

